Biogeosciences

Supplement of

Benthic silicon cycling in the Arctic Barents Sea: a reaction–transport model study

James P. J. Ward et al.

Correspondence to: James P. J. Ward (jamespj.ward@bristol.ac.uk)

S1 Introduction

This supplementary information comprises detailed descriptions of the Biogeochemical Reaction Network Simulator (BRNS), adapted for the benthic silica cycle and of the proposed Barents Sea Si budget. Here we also present additional model output figures, including the best-fit steady state simulation for station B14 and alternative fits for stations B13 and B15, wherein a heavier isotopic composition of the silicon (Si) phase desorbing from solid iron (Fe) (oxyhydr)oxides can reproduce the subtle continued increase in sediment pore water dissolved silicic acid (DSi) concentrations with depth.

S2 Biogeochemical Reaction Network Simulator

S2.1 Steady state model description

Reaction-transport models (RTMs) simulate and disentangle the complex interplay of chemical reactions and transport processes in sediments. Through use of an array of boundary conditions, a virtual sediment core can be placed in a real world context and used to fit laboratory data, from which it becomes possible to discern further information from concentration and isotopic measurements. For the early diagenesis of silica, this can prove useful as RTMs allow for the quantification of precipitation and dissolution reaction pathways, which can be difficult to constrain. Data-model best-fits were obtained by minimising RMSE (equation S1) between the predicted and observed values (Table S1).

$$RMSE = \sqrt{\frac{1}{n}\sum_{i=1}^{n}(x_i - x_i)^2} \tag{S1}$$

where i refers to variable i, n is the number of data points, x_i is the observational data and x_i represents the simulated data.

The Biogeochemical Reaction Network Simulator (BRNS) is an adaptive simulation environment suitable for large, mixed kinetic-equilibrium reaction networks (Regnier et al., 2002, 2003; Aguilera et al., 2005). A comprehensive list of boundary conditions and model parameters can be found in Table S2. This model assumes a steady state depositional dynamic and therefore does not resolve seasonal or transient dynamics without modification. BRNS is based on the vertically-resolved mass conservation equation S2 (Boudreau, 1997), which simulates concentration changes for solid and dissolved species (i) in porous media at each depth interval and time step:

$$\frac{\delta \sigma C_i}{\delta t} = \frac{\delta}{\delta z}\left(D_{bio}\sigma\frac{\delta C_i}{\delta z} + D_i\sigma\frac{\delta C_i}{\delta z}\right) - \frac{\delta \sigma \omega C_i}{\delta z} + \alpha_i\sigma(C_i(0) - C_i) + \sum_j \lambda_i^j R_j, \tag{S2}$$

where ω, C_i, t and z represent the sedimentation rate, concentration of species i, time and depth respectively. The porosity term σ is given as $\sigma = (1 - \varphi)$ for solid species, whereas for dissolved species $\sigma = \varphi$, where φ is sediment porosity. This term ensures that the respective concentrations represent the amount or mass per unit volume of porewater or solids as required (Boudreau, 1997). Porosity is attenuated exponentially with depth to account for sediment compaction, following (Mogollón et al., 2012):

$$\varphi_z = \varphi_x + (\varphi_0 - \varphi_x)e^{-z\cdot\beta} \tag{S3}$$

where φ_z and φ_0 is the porosity at depth z and the surface respectively, φ_x refers to porosity at the base of the core and β is the attenuation coefficient. φ_0 and φ_x were determined for each core and depth interval of Barents Sea sediments alongside this study and values for β were established based on best-fits of equation S3 to that data. D_{bio} is the bioturbation coefficient, which is modelled as a diffusive process (cm^2 yr^{-1}) and was determined experimentally for ChAOS stations along with the

Table S1. Goodness of fit measures between observational and simulated data. RMSE given in μM and ‰ for DSi and δ^{30}Si respectively. Normalised RMSE (NRMSE) is dimensionless, calculated by dividing RMSE by the difference between the maximum and minimum values.

	B13			**B14**			**B15**		
	RMSE	NRMSE	r^2	RMSE	NRMSE	r^2	RMSE	NRMSE	r^2
DSi	13.9	0.12	0.73	19.0	0.16	0.67	10.8	0.12	0.84
δ^{30}Si	0.16	0.12	0.83	0.30	0.13	0.87	0.21	0.11	0.60

maximum depth of mixing (4.9 $\pm$1.4 cm at B13 and B14; 6.4 $\pm$1.6 cm at B15) (Solan et al., 2020). D_i is the effective molecular
35 diffusion coefficient ($D_i = 0$ for solids) for dissolved species i. D_i values for ^{28}Si and ^{30}Si measured in 2°C seawater were taken from Rebreanu et al. (2008) and corrected for sediment tortuosity (θ^2) to produce D_{sed} (Boudreau, 1996). D_i varies with temperature (T) and viscosity (η), which was calculated with equation S4 (Rebreanu et al., 2008), using core top water temperatures measured at each station.

$$D_{sw} = 3.33 \times 10^{-12} \cdot (T \, / \, \eta) \qquad (S4)$$

40 Sedimentation rates are relatively poorly constrained in the Barents Sea (Freitas et al., 2020), with estimates ranging from 0.04-2.1 mm yr^{-1} based on ^{14}C (10-50 cm), ^{210}Pb and ^{137}Cs ($\leq$20 cm below the seafloor) analysis (Knies and Stein, 1998; Elverhøi, 1984; Elverhøi and Solheim, 1983; Zaborska et al., 2008; Carroll et al., 2008; Smith et al., 1995; Maiti et al., 2010; Faust et al., 2020). Given that measurements of DSi concentration and the isotopic compositions were determined only in the upper 30 cm of seafloor sediment, here we utilise ^{210}Pb sedimentation rate estimates from stations largely consistent with the
45 localities of B13, B14 and B15.

Unlike for bioturbation, the bioirrigation rate (α_i, yr^{-1}) for dissolved species ($\alpha_i = 0$ for solid species) was not experimentally determined alongside this study. Instead we implement a global mean value for the coefficient itself and also for its attenuation depth (x_{irr}) (Freitas et al., 2020; Thullner et al., 2009). We assume an attenuation depth of 3.5 cm, which typically irrigates sediment down to 15 cm depth (Thullner et al., 2009). The bioirrigation rate is determined from the coefficient applied
50 at the surface (equation S5) and describes exchange between the sediment-water interface (SWI) and the pore water below, which is defined as a 'nonlocal' process, i.e. transport of material occurs between points that are not adjacent to eachother (Boudreau, 1997). $\sum_j R_j$ represents the sum of the reactions (j) of reaction rate R_j within the implemented network that are either consuming or producing species i, while λ_i^j is the stoichiometric coefficient of species i for reaction j.

$$\alpha = \alpha_0 \cdot e^{\left(\frac{-z}{x_{irr}}\right)} \qquad (S5)$$

55 Mass conservation equation S2 is discretised spatially through use of a one dimensional finite-differencing mechanism (Thullner et al., 2009) over an irregular grid of 101 nodes (Boudreau, 1997), representing 50.4 cm of sampled core depth. Depth intervals are resolved at 0.1 cm to 3 cm depth, 0.2 cm to 5 cm, 0.4 cm to 10 cm, 0.6 cm to 20 cm and finally 1 cm intervals to 50 cm below the seafloor.

To summarise, equation S2 simulates concentration changes for solid and dissolved species in porous media at each depth
60 interval and time step, caused by multiple processes, including: sediment accumulation and compaction, molecular diffusion, macroinfaunal mixing (bioturbation and bioirrigation) and the consumption or production of species as defined by the user implemented reaction network.

S2.2   Reaction network and isotopic fractionation

The version of Si-BRNS employed in this study is similar to that found in Cassarino et al. (2020), which largely follows the
65   approach of Ehlert et al. (2016). The model accounts for a pool of sediment pore water DSi (as DSi_{30} and DSi_{28}) and biogenic
silica (as BSi_{30} and BSi_{28}). We assume that the total abundance of Si is accounted for by ^{28}Si and ^{30}Si (95.3%).

   In order to simulate the isotopic fractionation of Si due to early diagenetic processes, the model upper boundary conditions
(at the SWI) require the concentration of the isotopes ^{28}Si and ^{30}Si in mol cm^{-3} of the implemented phases. Through the mea-
sured isotopic composition of the modelled phases and the abundance ratios of the NBS-28 reference standard ($[Si_{29}]/[Si_{28}] =$
70   0.050745 and $[Si_{30}]/[Si_{28}] = 0.034147$, Ding et al. (2005)), it is possible to calculate the same ratios of the analysed material
through rearrangement of equation S6 (see equations S7 and S8). Subsequently, the concentration of each individual Si isotope
was calculated through a series of mass balance equations (equations S9-S12), which were used as upper boundary concentra-
tions. A no-flux condition was imposed for all species at the lower boundary of the model environment ($\delta C_i/\delta z = 0$), thereby
assuming that biogeochemical processes at greater depth do not influence the modelled domain.

75
$$\delta^{30}Si = \left(\frac{(^{30}Si/^{28}Si)_{sample}}{(^{30}Si/^{28}Si)_{NBS-28}} - 1 \right) \cdot 1000 \tag{S6}$$

$$\frac{[Si_{29}]}{[Si_{28}]}_{sample} = \left(\frac{\delta^{29}Si_{sample}}{1000} + 1 \right) \cdot \frac{[Si_{29}]}{[Si_{28}]}_{standard} \tag{S7}$$

$$\frac{[Si_{30}]}{[Si_{28}]}_{sample} = \left(\frac{\delta^{30}Si_{sample}}{1000} + 1 \right) \cdot \frac{[Si_{30}]}{[Si_{28}]}_{standard} \tag{S8}$$

$$\frac{[Si_{28}]}{[Si_{tot}]} + \frac{[Si_{29}]}{[Si_{tot}]} + \frac{[Si_{30}]}{[Si_{tot}]} = 1 \tag{S9}$$

$$\frac{\frac{[Si_{28}]}{[Si_{tot}]} + \frac{[Si_{29}]}{[Si_{tot}]} + \frac{[Si_{30}]}{[Si_{tot}]}}{[Si_{28}]} = \frac{1}{[Si_{28}]} \tag{S10}$$

80
$$\therefore [Si_{28}] = \frac{1}{\frac{1}{[Si_{tot}]} + \frac{1}{[Si_{tot}]} \cdot \left(\frac{[Si_{29}]}{[Si_{28}]} + \frac{[Si_{30}]}{[Si_{28}]} \right)} \tag{S11}$$

$$\therefore [Si_{29}] = [Si_{tot}] - [Si_{28}] - \left([Si_{28}] \cdot \frac{[Si_{30}]}{[Si_{28}]} \right) \tag{S12}$$

   Following Ehlert et al. (2016) and Cassarino et al. (2020), the model used in this study accounts for a pool of pore water DSi,
sourced by a dissolving BSi phase, from which Si can be incorporated into authigenic clay minerals as they precipitate ($AuSi_{30}$
and $AuSi_{28}$), thereby inducing a fractionation on the DSi phase. The Si isotopic fractionation factor ($^{30}\epsilon$) associated with clay
85   mineral precipitation is relatively high (-1.8 to -2.2 ‰) (Hughes et al., 2013; Ziegler et al., 2005a, b; Opfergelt and Delmelle,
2012). The kinetic rate law for the dissolution of BSi follows equation S16 (Hurd, 1972), where k_{diss} is the reaction rate
constant (yr^{-1}) and BSi_{sol} is the solubility of BSi (mol cm^{-3}), therefore stating that the rate is proportional to the saturation

state of the DSi phase. The rate of BSi dissolution is allowed to decrease exponentially downcore following equation S15, where ad is the attenuation coefficient and bd is the minimum reaction rate, in order to account for a reduction in reactivity due to maturation and interaction with dissolved Aluminium (Al), as well as the preferential dissolution of more reactive material at shallower depths (Rickert, 2000; Van Cappellen and Qiu, 1997; Rabouille et al., 1997; Dixit et al., 2001). While this study assumed that no isotopic fractionation occurs during BSi dissolution (α_d = 1.0) (Wetzel et al., 2014; Ehlert et al., 2016), equations S17 and S18 allow for an equilibrium fractionation to be induced if required, through use of the fractionation factor α_d. Indeed, previous work has shown that BSi dissolution can sometimes induce a slight fractionation that enriches the DSi pool in the lighter isotope ($^{30}\epsilon$ of -0.55 ‰) (Demarest et al., 2009).

$$fb_{30} = \frac{BSi_{30}}{BSi_{30} + \alpha_d \cdot BSi_{28}} \tag{S13}$$

$$fb_{28} = \frac{\alpha_d \cdot BSi_{28}}{BSi_{30} + \alpha_d \cdot BSi_{28}} \tag{S14}$$

$$fb_z = e^{-ad \cdot x_{pos}} + bd \tag{S15}$$

$$R_{db} = k_{diss} \cdot fb_z \cdot (BSi_{30} + BSi_{28}) \cdot \left(1.0 - \frac{(DSi_{30} + DSi_{28})}{BSi_{sol}}\right) \tag{S16}$$

$$R_2 = fb_{30} \cdot R_{db} \tag{S17}$$

$$R_3 = fb_{28} \cdot R_{db} \tag{S18}$$

An additional two reaction pathways have been introduced into our model relative to those of Cassarino (2018) and Ehlert et al. (2016), which are the dissolution of a lithogenic phase (LSi_{30} and LSi_{28}) and two reaction rates representing the release of DSi_{30} and DSi_{28} from solid phase Fe (oxyhydr)oxides. As is the case for BSi, LSi dissolution is assumed to be dependent upon the degree of pore water DSi undersaturation and follows equation S21, where $k_{LSidiss}$ is the dissolution rate constant and LSi_{sol} represents the solubility of the lithogenic phase. Lerman et al. (1975) determined during a dissolution experiment of common silicate minerals that the reaction could be described by a first-order rate law, driven by the saturation state. The concentration of LSi (LSi_{28} and LSi_{30}) was determined based on sedimentary bulk Si contents measured by wavelength dispersive X-ray fluorescence (XRF) of the 0-0.25 cm sediment core depth interval: 26.1, 24.7 and 23.3% Si at stations B13, B14 and B15 respectively.

For XRF analysis, sample splits of 700 mg was mixed with 4200 mg di-lithiumtetraborate ($Li_2B_4O_7$, Spectromelt A10), preoxidized at 500°C with 1.0 g NH_4NO_3 (p.a.) and fused to homogenous glass beads. The glass beads were analysed using a Philips PW-2400 WD-XRF spectrometer calibrated with 53 geostandards at the University of Oldenburg. Analytical precision and accuracy were better than 5%, as checked by in-house and international reference materials. Bulk sediment Si contents were then corrected for the BSi component, assuming that almost all of the solid phase is composed of terrigenous material. Ward et al. (2022) determined that approximately 96% of Barents Sea surface sediments are terrigenous in origin, estimated using the following equation (Sayles et al., 2001):

$$\%Terrigenous = 100 - \%(BSi + CaCO_3 + TOC) \tag{S19}$$

where TOC refers to total organic carbon content of the surface sediment interval.

The LSi dissolution rate is set to decrease exponentially with depth, following equation S20, where al is the attenuation coefficient, bl represents the minimum rate and x_{pos} is depth. This exponential reduction in rate is imposed because the uppermost sediment layers are thought to be where the majority of dissolved Al sourced from LSi dissolution is released in marine sediments (Van Beusekom et al., 1997; Ehlert et al., 2016; Geilert et al., 2020). We have assumed there is no isotopic fractionation during the dissolution of LSi.

$$fl_z = e^{-al \cdot x_{pos}} + bl \tag{S20}$$

$$R_{dl} = k_{LSidiss} \cdot fl_z \cdot (LSi_{30} + LSi_{28}) \cdot \left(1.0 - \frac{(DSi_{30} + DSi_{28})}{LSi_{sol}}\right) \tag{S21}$$

The desorption of DSi from solid phase Fe (oxyhydr)oxides as they reductively dissolve under anoxic conditions was modelled through two reaction rate constants, representing the release of DSi_{30} (k_{FeSi30}) and DSi_{28} (k_{FeSi28}) from the solid phase (equations S22-S23). This parameter likely represents a significant simplification, however the exact process pertaining to the adsorption of Si onto Fe (oxyhydr)oxides is unclear and requires further study (Geilert et al., 2020). Adsorption of Si onto Fe (oxyhydr)oxides preferentially takes up the lighter isotope, the degree to which is thought to increase with mineral crystallinity ($^{30}\epsilon$ of -1.06 ‰ for ferrihydrite and -1.59 ‰ for goethite) (Delstanche et al., 2009). Furthermore, Ward et al. (2022) presented evidence for the presence of an isotopically light metal oxide phase, through analysis of weak acid leachates used to extract solid phase reactive Si pools (-2.88 ±0.17 ‰). The implemented ratio of k_{FeSi30} and k_{FeSi28} in the model reflects the composition of this reactive pool.

Step-functions (SW03 and SW04) were implemented in the FeSi reactions in the model to simulate the desorption of this phase at specific depth intervals, representing the Fe redox boundaries identified in Ward et al. (2022). The step-functions act as a cut-off mechanism, either setting reaction rates to zero or activating them at specific depths. Release of the FeSi phase was ceased at a particular depth interval, determined based on the best-fit between the simulated and measured data.

$$R_7 = SW03 \cdot SW04 \cdot k_{FeSi28} \tag{S22}$$

$$R_8 = SW03 \cdot SW04 \cdot k_{FeSi30} \tag{S23}$$

The precipitation of authigenic clay minerals ($AuSi_{30}$ and $AuSi_{28}$) was modelled with equation S27, where k_{precip} represents the authigenic rate constant (Ehlert et al., 2016). This rate law states that the reaction will proceed, providing the concentration of DSi is greater than the solubility of the authigenic phase ($AuSi_{sol}$). The rate is thus proportional to the degree of pore water DSi oversaturation (Ehlert et al., 2016). As with BSi dissolution, the rate of AuSi precipitation was allowed to decrease exponentially with depth through equation S26, where ap is the attenuation coefficient and bp is the minimum rate. This reduction in reaction rate with depth accounts for the general consensus that the majority of authigenic clay mineral precipitation occurs in the upper portion of marine sediment cores. Here, DSi can more easily precipitate in the presence of dissolved Al, the concentration of which is typically higher in the upper reaches of shelf sediments, sourced from the dissolution of reactive LSi minerals (e.g. feldspar and gibbsite) contemporaneous to that of BSi (Aller, 2014; Rabouille et al., 1997; Van Beusekom et al., 1997; Ehlert et al., 2016). Fractionation of the dissolved phase associated with clay mineral precipitation is accounted for by equations S28 and S29, through the fractionation factor α_p.

$$fp_{30} = \frac{DSi_{30}}{DSi_{30} + \alpha_p \cdot DSi_{28}} \tag{S24}$$

$$fp_{28} = \frac{\alpha_p \cdot DSi_{28}}{DSi_{30} + \alpha_p \cdot DSi_{28}} \tag{S25}$$

155 $\quad fp_z = e^{-ap \cdot x_{pos}} + bp \tag{S26}$

$$R_p = SW02 \cdot k_{precip} \cdot fp_z \cdot \left(\frac{(DSi_{30} + DSi_{28})}{AuSi_{sol}} - 1.0 \right) \qquad \text{if } [DSi] > AuSi_{sol} \tag{S27}$$

$$R_{10} = fp_{30} \cdot R_p \tag{S28}$$

$$R_{11} = fp_{28} \cdot R_p \tag{S29}$$

Table S2: BRNS transport and reaction parameters and boundary conditions for the best-fit steady state model simulations. Values are 'independent' (I) if based on laboratory or fieldwork measurements, 'constrained' (C) if potential values could be bracketed or calculated from an empirical relationship, or finally 'model-derived' (M). *Lerman et al. (1975) determined that glauconite, a common aluminosilicate reverse weathering product of BSi has a solubility of $\sim$50 μM in seawater at low temperatures. Hurd (1973) calculated that sepiolite, an authigenic clay mineral that forms on BSi could precipitate from sediment pore waters with a DSi as low as 30 μM. [†] Zhu et al. (2016) observed fractionation factors ($^{30}\epsilon$) of -2.87 to +0.80 ‰, averaging -0.995 $\pm$1.16 ‰ (1σ) during albite dissolution, with the DI water solution becoming enriched in the lighter isotope. However, the magnitude of $^{30}\epsilon$ was found to be dependent on pH and was much lower at pH 7 (averaging 0.11 $\pm$0.98 ‰).

Parameter	Unit	Type	B13	B14	B15	Source
General						
L	cm	-	50.4	50.4	50.4	-
nNodes	-	-	101	101	101	-
Run time	yr	-	2600	3000	3000	-
T	^oC	I	1.78	1.9	-1.49	-
S	PSU	I	35.014	35.01	35.9	-
Depth	m	I	359	293	317	-
φ_0	-	I	0.83	0.89	0.90	-
φ_x	-	I	0.62	0.65	0.65	-
β	-	I	0.10	0.105	0.105	-
Transport						
D_{bio}	cm^2 yr^{-1}	I	6.1	3.9	1.9	-
x_{bio}	cm	I	2.0	2.0	2.0	-
α_0	yr^{-1}	C	10	10	10	Thullner et al. (2009)
x_{irr}	cm	C	3.5	3.5	3.5	Thullner et al. (2009)
ω	cm yr^{-1}	C	0.05	0.05	0.06	Zaborska et al. (2008)
$D_{sed^{28}Si}$	cm^2 yr^{-1}	C	125	127	128	Rebreanu et al. (2008)
$D_{sed^{30}Si}$	cm^2 yr^{-1}	C	125	127	128	Rebreanu et al. (2008)
Reaction						
$[DSi_{28}]$	μmol Si cm^{-3}	I	0.00645	0.00829	0.00553	-
$[DSi_{30}]$	μmol Si cm^{-3}	I	0.00022	0.00028	0.00019	-
$[BSi_{28}]$	μmol Si cm^{-3} solid	I	$3.22\cdot10^2$	$4.27\cdot10^2$	$2.12\cdot10^2$	-
$[BSi_{30}]$	μmol Si cm^{-3} solid	I	$1.1\cdot10^1$	$1.46\cdot10^1$	7.23	-
$\delta^{30}Si_{DSi}$	‰	I	1.64	1.46	1.69	-
$\delta^{29}Si_{DSi}$	‰	I	0.84	0.8	0.89	-
$\delta^{30}Si_{BSi}$	‰	I	1.43	1.5	0.82	-
$\delta^{29}Si_{BSi}$	‰	I	0.71	0.76	0.39	-
$\delta^{30}Si_{LSi}$	‰	I	-0.89	-0.89	-0.89	-
$\delta^{29}Si_{LSi}$	‰	I	-0.49	-0.49	-0.49	-
$\delta^{30}Si_{FeSi}$	‰	I	-2.88	-2.88	-2.88	-

$\delta^{29}Si_{FeSi}$	‰	I	-1.46	-1.46	-1.46	-
BSi_{sol}	μM	C	800	800	800	Van Cappellen et al. (2002)
LSi_{sol}	μM	C	95	100	95	See Table S3
$AuSi_{sol}$	μM	C	50	50	50	Lerman et al. (1975); Hurd (1973)*
k_{diss}	yr^{-1}	M	$0.55 \cdot 10^{-2}$	$7.4 \cdot 10^{-2}$	$1.05 \cdot 10^{-2}$	-
$k_{LSidiss}$	yr^{-1}	M	$200 \cdot 10^{-4}$	$500 \cdot 10^{-5}$	$300 \cdot 10^{-5}$	-
k_{precip}	mol Si cm^{-3} yr^{-1}	M	$0.65 \cdot 10^{-4}$	$0.6 \cdot 10^{-5}$	$4.5 \cdot 10^{-5}$	-
$k_{FeSi_{28}}$	mol Si cm^{-3} yr^{-1}	M	$1.44 \cdot 10^{-6}$	$5.578 \cdot 10^{-8}$	$5.578 \cdot 10^{-8}$	-
$k_{FeSi_{30}}$	mol Si cm^{-3} yr^{-1}	M	$4.903 \cdot 10^{-8}$	$1.899 \cdot 10^{-9}$	$1.899 \cdot 10^{-9}$	-
α_d	-	C	1.0	1.0	1.0	Wetzel et al. (2014)
α_p	-	C	1.0023	1.002	1.0023	Opfergelt and Delmelle (2012)
α_l	-	C	1.0	1.0	1.0	Zhu et al. (2016)[†]
ad	-	M	0.2	0.42	0.4	-
al	-	M	0.2	0.01	0.05	-
ap	-	M	0.65	0.85	0.35	-
bd	yr^{-1}	M	0.05	0.0	0.0	-
bl	yr^{-1}	M	6.0	1.5	6.0	-
bp	mol Si cm^{-3} yr^{-1}	M	0.05	0.0065	0.0001	-

S3   A proposed Si budget for the Barents Sea

160 An isotopic assessment of the Arctic Ocean Si budget has highlighted the requirement for an additional sink of light Si, if isotopic balance is to be attained (Brzezinski et al., 2021). Here we build on this work by combining isotopic analysis of the water column and the dissolved and solid phases of the sediment (Ward et al., 2022), with reaction-transport modelling carried out in this study, to present an isotopically balanced Si budget for the Barents Sea that may help to inform the pan-Arctic Ocean equivalent.

165 The Si inflow rate from Atlantic Waters crossing the Barents Sea Opening is 0.42 ±0.07 Tmol Si yr^{-1} (Torres-Valdés et al., 2013), while the outflow rate through the northern openings (the Barents Sea Exit between Novaya Zemlya and Franz Josef Land, as well as the Franz Victoria Trough (Fig. 1)) estimated here is 0.35 Tmol Si yr^{-1}. This outflow was calculated by integrating the water column DSi depth profiles of the northernmost ChAOS stations (B16 and B17) and similar profiles measured during the ARK IX/4 cruise on the Barents Sea side of the shelf break (PS27/006-1, PS27/026-1 and

170 PS27/027-1, Luchetta et al. (2021)). All water column nutrient data for JR16006 (doi:10.5285/b4c1537e-c729-6463-e053-6c86abc0c7de), JR17006 (doi:10.5285/b62f2d5d-1f40-0c2c-e053-6c86abc0265d) and JR18006 (doi:10.5285/cc1dec98-40b5-5c51-e053-6c86abc01a6d) is available at the British Oceanographic Data Centre (BODC). The average depth-integrated DSi concentration (4.8 μM) was then multiplied by the Barents Sea volumetric outflow rate (2.3 Sv) (Smedsrud et al., 2013). Unlike the Arctic Ocean as a whole, which is a slight net exporter of Si with respect to the main inflow and outflow water masses

175 (Brzezinski et al., 2021), the Barents Sea appears to be a slight net importer. However, our calculations are based on DSi water column profiles sampled from the lesser of two Barents Sea outflow locations. The main outflow gateway, between Novaya Zemlya and Franz Josef Land, is also north of the oceanic polar front and dominated by the Arctic Water mass (Fig. 1), therefore we would not expect a significant difference in DSi water column profiles between the two localities. Nevertheless we cannot be certain of the Barents Sea Si outflow rate without concentration data from the eastern side of the shelf. Consistent with the

180 wider Arctic Ocean Si budget, the δ^{30}Si of the core top water from the Arctic (B15) and Atlantic Water (B13) stations, range from +1.64 to +1.69 ‰ (Ward et al., 2022), assumed here to represent the main outflow and inflow water masses respectively.

The riverine DSi influx presented in Fig. 6 (2580×10^3 tSiO$_2$ yr^{-1}, or 0.044 Tmol Si yr^{-1}), represents the sum of the four main rivers draining into the Barents and White Seas, including the Onega, Northern Dvina, Mezen and the Pechora (Gordeev et al., 1996). The estimated average δ^{30}Si of the fluvial flux to the Arctic Ocean is 1.3 ±0.3 ‰, but varies temporally by season and spatially from +0.86 ±0.3 ‰ in the Lena to +1.6 ±0.25 ‰ in the Yenisey River, which flow into the Laptev and Kara Seas respectively (Sun et al., 2018).

The benthic flux of DSi has been recategorised in our budget of the Barents Sea, relative to that of Brzezinski et al. (2021), reflecting the conclusions drawn from our reaction-transport model study. Here we assume that between 60 and 98% of the benthic DSi flux is sourced from the dissolution of LSi, which represents an input of new Si into the Barents Sea Si budget, while the remainder constitutes an internal recycling flux (i.e. the dissolution of BSi). Therefore, the contribution of LSi to the influx of Si to the Barents Sea, assuming an average benthic flux of +0.23 ±0.11 mmol Si m^{-2} d^{-1} and a shelf seafloor area of 1.4 million km^{-2}, ranges from 0.07 to 0.115 Tmol Si yr^{-1}. A δ^{30}Si of -0.88 ‰ for the dissolving LSi phase is based on a series of sequential digestion experiments carried out on the surface sediment interval collected from stations B13, B14 and B15 (Ward et al., 2022), but can range from -0.90 to +0.73 ‰ across primary silicates (felsic crustal and mafic mantle source rocks) and -2.9 to 0 ‰ for secondary clay minerals (Opfergelt and Delmelle, 2012) (mean -1.07 ‰, Sutton et al. (2018)).

The two outputs in the biogeochemical cycle of Si in the Barents Sea seafloor, outside of the main water mass outflow, are the burial of AuSi and BSi. The burial of BSi (0.0123 Tmol Si yr^{-1}) is calculated in section 3.4 of the main text, based on an asymptotic BSi content of 0.2 wt% below the mid-core at all three stations, assumed to be controlled solely by advection due to sediment accumulation (corrected for compaction). The same equation was used to calculate the burial rate of AuSi across the shelf (0.018-0.24 Tmol Si yr^{-1}), based on the simulated concentration at the base of the model domain at stations B14 and B15 (0.32 and 4.8 wt% respectively). The AuSi concentration at depth in the model for station B13 (12 wt%) is much higher than that at B14 and B15, consistent with the increased depth-integrated reaction rate (Table 2), corresponding to a burial rate of 0.87 Tmol Si yr^{-1}. This AuSi burial rate far outweighs the sum of the inputs to the Barents Sea, which would lead to a significant imbalance in the Si budget if it were considered a reasonable value with which to scale up our calculations. We therefore employ the values at stations B14 and B15 as conservative estimates for AuSi burial in the Barents Sea in our calculations, as B13 likely represents a site of localised, elevated AuSi precipitation. Alternatively, there could be a complexity that our model does not adequately capture for this station, leading to an overestimated AuSi precipitation rate. The δ^{30}Si of the buried BSi phase is assumed to be the same as the composition measured in the surface sediments, determined from sequential digestion experiments (+0.82 to +1.50 ‰, Ward et al. (2022)). For the mass balance calculations, the composition of the AuSi phase was assumed to be -1.07 ‰, based on the average composition of secondary minerals (Sutton et al., 2018), however this can range from -2.9 to ~0 ‰ (Opfergelt and Delmelle, 2012).

Disregarding the main water mass in and outflows, our Si budget suggests an influx to the Barents Sea of 0.11-0.16 Tmol Si yr^{-1} at -0.39 to +0.08 ‰ and an outflow of 0.03-0.25 Tmol Si yr^{-1} at -0.97 to -0.03 ‰, with the potential for the higher outflux to account for the slight mass imbalance between the water mass inflow and outflow (0.12 Tmol Si yr^{-1}). Our Si budget of the Barents Sea therefore demonstrates that through the re-categorisation of the benthic flux term and the introduction of AuSi burial, we are able to achieve isotopic and mass balance.

S4 Sediment pigment extraction methodology

Samples of surface sediment (2–3 g) were thawed and centrifuged (Eppendorf, 4000 rpm, 5 min, 4 ^{o}C) to remove excess water. Sediment was then transferred to a pre-weighed extraction tube to which 3 mL of 100% acetone was added. Extracts were kept on ice and in the dark during extraction. Samples were sonicated (Sonics Vibracell probe, 50 s, 40 W), then left on ice to soak for 1 hr before centrifugation (Eppendorf, 4000 rpm, 5 min, 4 ^{o}C), and the supernatant decanted. The procedure was repeated until extracts appeared colourless. Samples were filtered prior to HPLC (0.2 μm, 17 mm Teflon syringe filters, DHI, Denmark). Samples were injected on an Agilent 1200 HPLC system running an HPLC method for sedimentary pigments (Airs

et al. (2001), Method C). The Agilent 1200 system comprised a G1312A binary pump, a G1376B thermostated autosampler, a thermostated column compartment and a G1315B photodiode array detector. Pigment extracts (80 μL) were mixed with MilliQ water (8 μL) in the autosampler and injected onto the HPLC column (2 Waters Spherisorb ODS2 cartridges coupled together, each 150 x 4.6 mm, particle size 3 μm, protected with a precolumn containing the same phase). Extracts were maintained in the dark at 4 ^{o}C in the autosampler, and were analysed within 24 hr of extraction. Injection of a mixed standard (DHI Denmark) was performed to check pigment resolution prior to analysis of samples. Chlorophyll and its degradation products were quantified according to response factors calculated from injection of standards (DHI, Denmark). For quantification of hydroxychlorophyllone, the response factor for pheophorbide a was used as the two components have similar UV/vis absorbance spectra (Airs et al., 2001), and no standard was available for hydroxychlorophyllone. Selected sediment samples were analysed by LC/MS^{n} for assignment of components (Airs et al., 2001). LC/MS^{n} was performed using an Agilent 6330 ion trap mass spectrometer via an atmospheric pressure chemical ionisation (APCI) source. MS settings were as follows: Ionisation mode: positive, drying temperature 350 ^{o}C, vaporiser temperature 450 ^{o}C, nebuliser pressure 60 PSI, drying gas flow rate 5 L/min. The scan range was m/z 400–1100. Post column addition of acid was used to aid ionisation of metallated components (Airs and Keely, 2000). Components were assigned based on relative retention time, on-line UV/vis spectra, protonated molecule and fragmentation data (Airs et al., 2001).

For schematic Fig. 2 of the main text, we have assumed that a shift from fucoxanthin (fuco)-dominated surface sediments to those containing both fuco and hexanoyoxyfucoxanthin (hex-fuco) represents a switch from diatom to haptophyte-dominated (e.g. *E. huxleyi* or *Phaeocystis*) material. Fuco is the more common of the two and the dominant pigment of diatoms, while hex-fuco is typical of *Phaeocystis* (Antajan et al., 2004). Therefore, the abundance of hex-fuco relative to fuco, can be used as a proxy to determine *Phaeocystis* prevalence (Antajan et al. (2004) and references therein).

Table S3: Solubility of primary and secondary silicates in seawater (SW). The Siever (1968) experiment was carried out in distilled water (DW).

Mineral	Solubility (μM)	Source	Conditions
Kaolinite	67	Siever (1968)	25 days, 25°C, DW
	64;83	Mackenzie et al. (1967)	375 days, room temp, SW
	50	Lerman et al. (1975)	8.5 years, Bermuda SW
	10-300	Hurd et al. (1979)	12 weeks, 1-2°C, SW
Montmorillonite	130; 183	Mackenzie et al. (1967)	
	100	Fanning and Schink (1969)	10 months, room temp, SW
	130;166	Lerman et al. (1975)	
	80-250	Hurd et al. (1979)	
Chlorite	33	Mackenzie and Garrels (1965)	10 months, room temp, SW
	70	Mackenzie et al. (1967)	
	30	Fanning and Schink (1969)	
	40-80	Hurd et al. (1979)	
Illite	95	Mackenzie et al. (1967)	
	100	Lerman et al. (1975)	
	40-70	Hurd et al. (1979)	
Muscovite	127	Mackenzie et al. (1967)	
	125	Lerman et al. (1975)	
Glauconite	60	Mackenzie et al. (1967)	
	50	Lerman et al. (1975)	
Bentonite	433		
	115-340	Hurd et al. (1979)	
Quartz	100	Lerman et al. (1975)	
Phillipsite	150		
Analcite	100		
Prehnite	92		
Albite	55-110		
Hornblende	50-120		
Nepheline	35-75		
Biotite	60-120		
Hypersthene	200-275		
Epidote	150-200		
Tremolite	200-275		
Olivine	300-700		
Bulk sediment			
Congo fan	48	Loucaides et al. (2010)	22 months, ocean mooring
Mississippi delta	46;52		
Basalt			

|			
River bedload	103	Jones et al. (2012)	9 months, 5°C, SW
Estuary sediment	129		
Volcanic glass	90	Staudigel et al. (1998)	314 days, room temp, SW
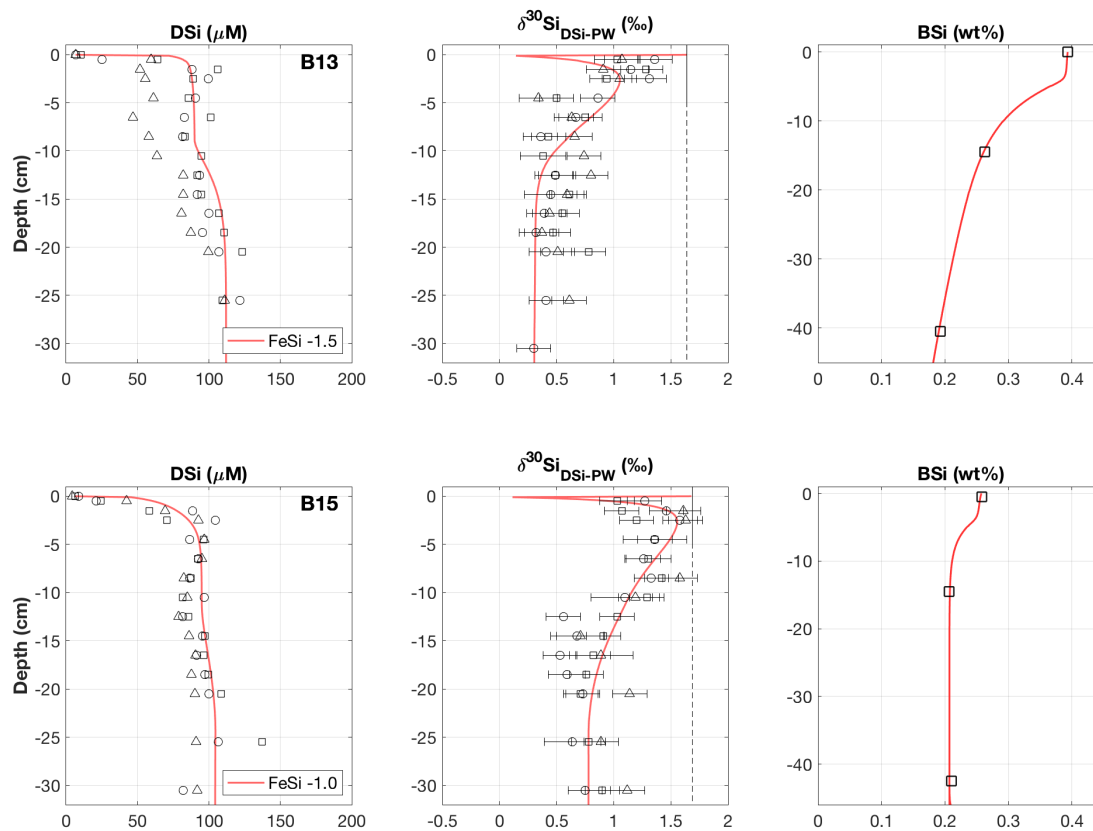
Figure S1. Best-fit model simulations (red line) with heavier FeSi compositions of -1.5 and -1.0 ‰ implemented at stations B13 and B15 respectively. The heavier composition of the desorbing phase allows for sufficient DSi release to resolve the slight increase in pore water DSi concentration from the mid-core to depth. Vertical dashed black lines represents the isotopic compositions of the core top waters from 2017.
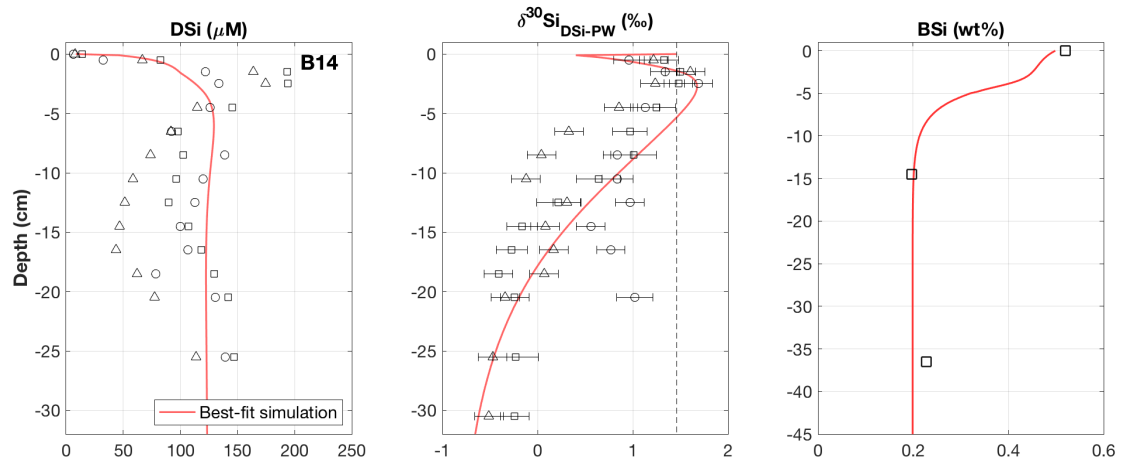
Figure S2. Best-fit model simulation station B14 (red line). Vertical dashed black line represents the isotopic composition of the core top water from 2017. BSi content was measured from samples collected in 2019. Model output was fit to the sediment pore water DSi concentrations from 2018 (open circles), as this profile is closer to the background steady state system than 2017 or 2019.
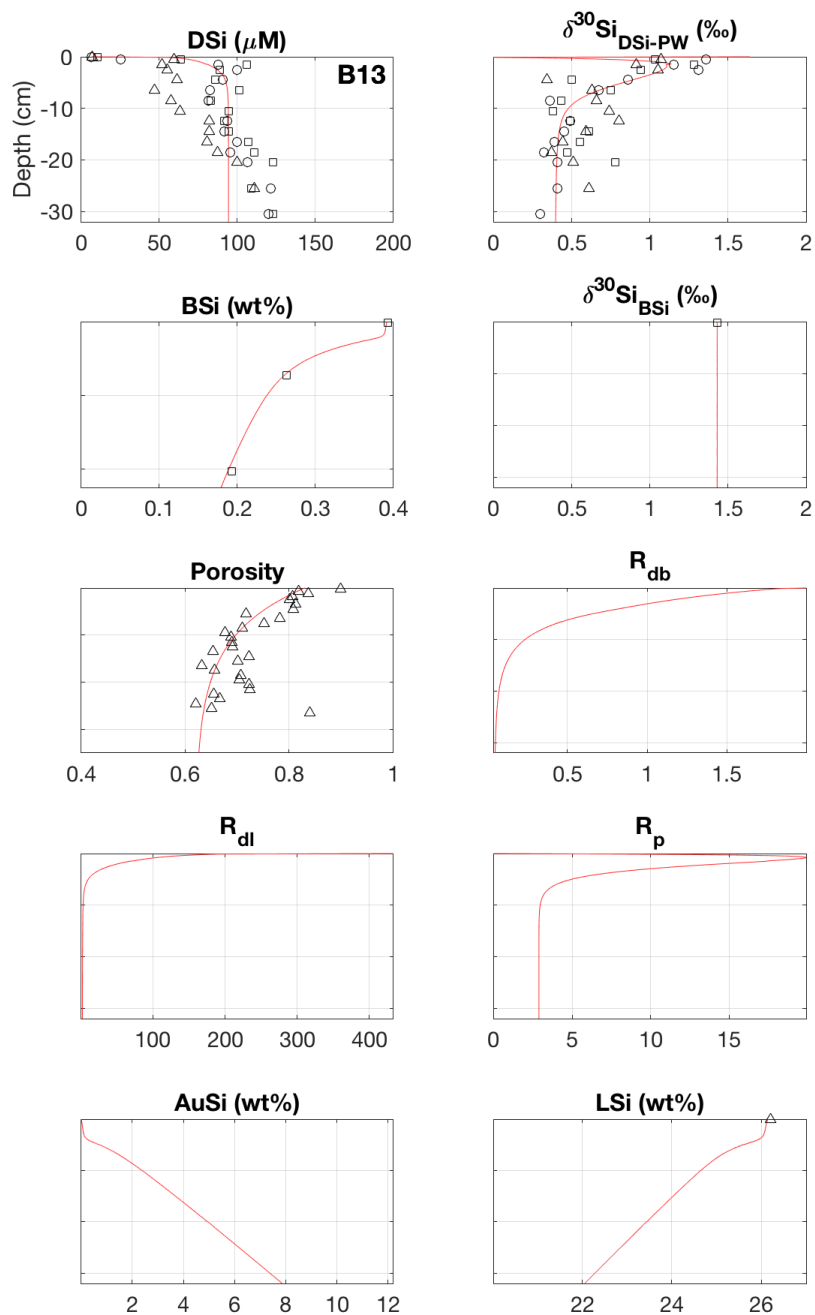
Figure S3. Model output summary (red lines) *vs* data (open shapes) from the best-fit simulation at station B13. R_{db}- rate of BSi dissolution, R_{dl}- rate of LSi dissolution, R_{p}- rate of AuSi precipitation. All reaction rates are given in μmol cm^{-3} yr^{-1}.
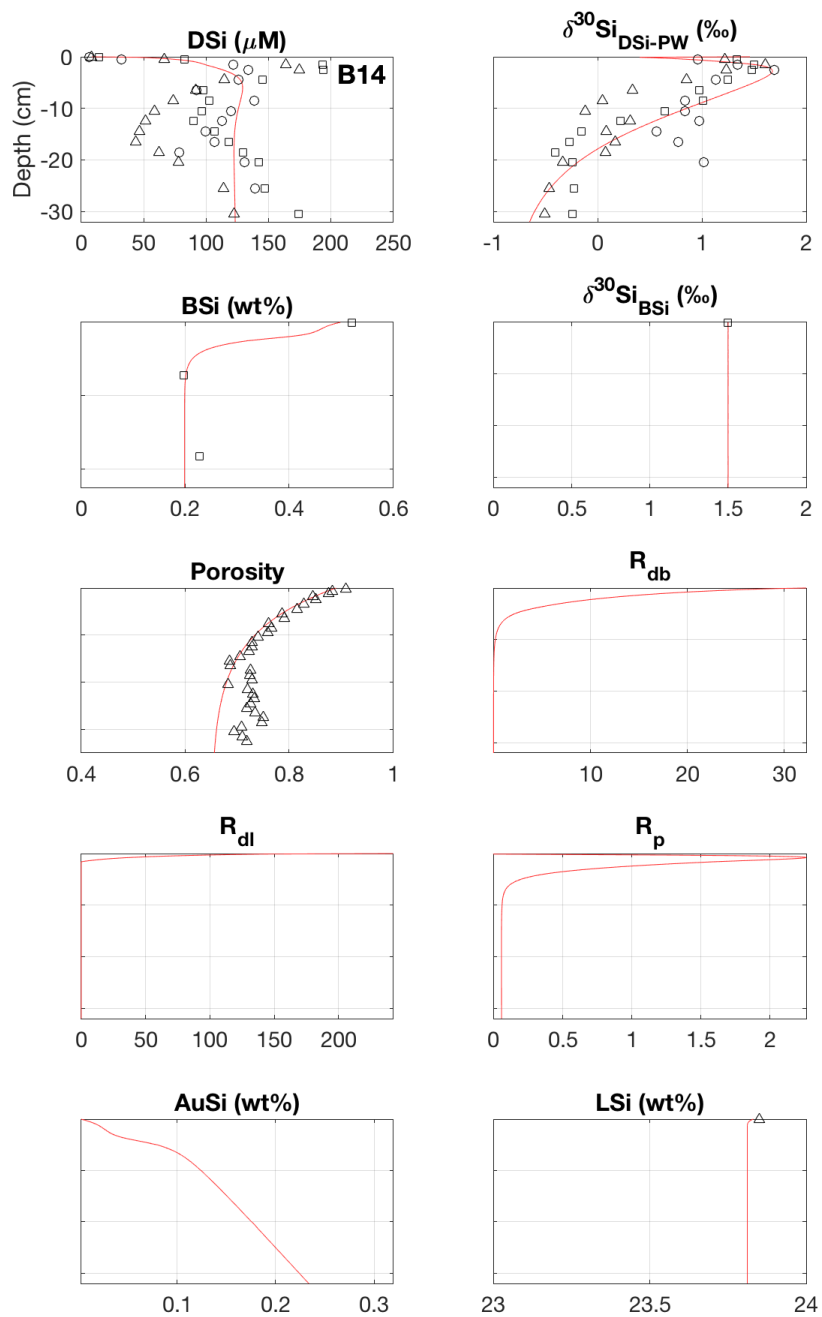
Figure S4. Model output summary (red lines) *vs* data (open shapes) from the best-fit simulation at station B14. All reaction rates are given in μmol cm^{-3} yr^{-1}.
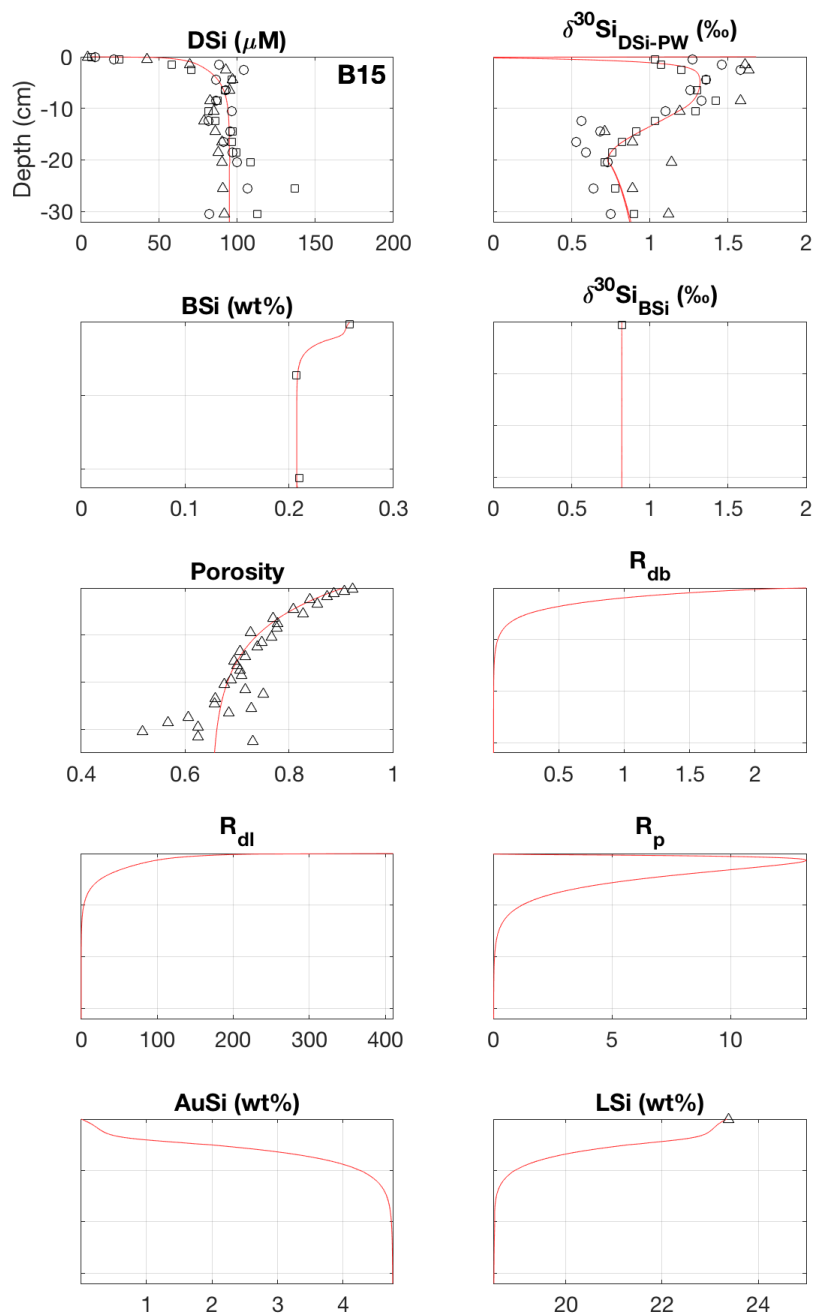
Figure S5. Model output summary (red lines) *vs* data (open shapes) from the best-fit simulation at station B15. All reaction rates are given in μmol cm^{-3} yr^{-1}.
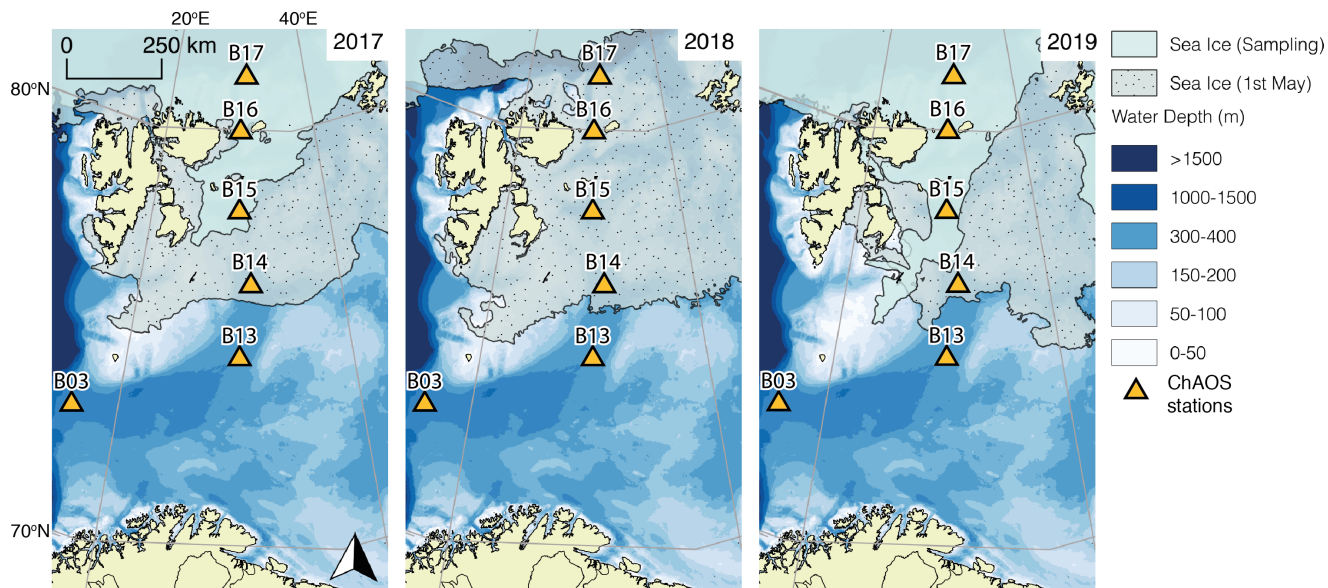
Figure S6. Sea ice conditions during sampling at station B14 (30/7/2017, 25/7/2018, 13/7/2019) *vs* May 1st of each year (Ward et al., 2022). Sea ice data from U.S. National Ice Center and National Snow and Ice Data Center (NSIDC) (Fetterer et al., 2010).

245

References

Aguilera, D. R., Jourabchi, P., Spiteri, C., and Regnier, P.: A knowledge-based reactive transport approach for the simulation of biogeochemical dynamics in Earth systems, Geochem. Geophys. Geosystems., 6, https://doi.org/10.1029/2004GC000899, 2005.

Airs, R. L. and Keely, B. J.: A novel approach for sensitivity enhancement in atmospheric pressure chemical ionisation liquid chromatography/mass spectrometry of chlorophylls, Rapid Commun. Mass Spectrom., 14, 125–128, https://doi.org/10.1002/(SICI)1097-0231(20000215)14:3<125::AID-RCM847>3.0.CO;2-6, 2000.

Airs, R. L., Atkinson, J. E., and Keely, B. J.: Development and application of a high resolution liquid chromatographic method for the analysis of complex pigment distributions, J. Chromatogr. A, 917, 167–177, https://doi.org/10.1016/S0021-9673(01)00663-X, 2001.

Aller, R. C.: 8.11 - Sedimentary Diagenesis, Depositional Environments, and Benthic Fluxes, Treatise on Geochemistry (Second Edition), 8, 293–334, https://doi.org/10.1016/B978-0-08-095975-7.00611-2, 2014.

Antajan, E., Chrétiennot-Dinet, M. J., Leblanc, C., Daro, M. H., and Lancelot, C.: 19′-Hexanoyloxyfucoxanthin may not be the appropriate pigment to trace occurrence and fate of Phaeocystis: The case of P. globosa in Belgian coastal waters, J. Sea Res., 52, 165–177, https://doi.org/10.1016/j.seares.2004.02.003, 2004.

Boudreau, B. P.: The diffusive tortuosity of fine-grained unlithified sediments, Geochim. Cosmochim. Acta, 60, 3139–3142, https://doi.org/10.1016/0016-7037(96)00158-5, 1996.

Boudreau, B. P.: Diagenetic models and their implementation: modelling transport and reactions in aquatic sediments, Springer, New York, 1st edn., 1997.

Brzezinski, M. A., Closset, I., Jones, J. L., de Souza, G. F., and Maden, C.: New Constraints on the Physical and Biological Controls on the Silicon Isotopic Composition of the Arctic Ocean, Front. Mar. Sci., 8, https://doi.org/10.3389/fmars.2021.699762, 2021.

Carroll, J. L., Zaborska, A., Papucci, C., Schirone, A., Carroll, M. L., and Pempkowiak, J.: Accumulation of organic carbon in western Barents Sea sediments, Deep. Res. II, 55, 2361–2371, https://doi.org/10.1016/j.dsr2.2008.05.005, 2008.

Cassarino, L.: From micro to macro: silicon isotope fractionation during biogenic opal formation, Ph.D. thesis, University of Bristol, 2018.

Cassarino, L., Hendry, K. R., Henley, S. F., MacDonald, E., Arndt, S., Freitas, F. S., Pike, J., and Firing, Y. L.: Sedimentary Nutrient Supply in Productive Hot Spots off the West Antarctic Peninsula Revealed by Silicon Isotopes, Global Biogeochem. Cycles, 34, https://doi.org/10.1029/2019GB006486, 2020.

Delstanche, S., Opfergelt, S., Cardinal, D., Elsass, F., André, L., and Delvaux, B.: Silicon isotopic fractionation during adsorption of aqueous monosilicic acid onto iron oxide, Geochim. Cosmochim. Acta, 73, 923–924, https://doi.org/10.1016/j.gca.2008.11.014, 2009.

Demarest, M. S., Brzezinski, M. A., and Beucher, C. P.: Fractionation of silicon isotopes during biogenic silica dissolution, Geochim. Cosmochim. Acta, 73, 5572–5583, https://doi.org/10.1016/j.gca.2009.06.019, 2009.

Ding, T., Wan, D., Bai, R., Zhang, Z., Shen, Y., and Meng, R.: Silicon isotope abundance ratios and atomic weights of NBS-28 and other reference materials, Geochim. Cosmochim. Acta, 69, 5487–5494, https://doi.org/10.1016/j.gca.2005.06.015, 2005.

Dixit, S., Van Cappellen, P., and Van Bennekom, A. J.: Processes controlling solubility of biogenic silica and pore water build-up of silicic acid in marine sediments, Mar. Chem., 73, 333–352, https://doi.org/10.1016/S0304-4203(00)00118-3, 2001.

Ehlert, C., Doering, K., Wallmann, K., Scholz, F., Sommer, S., Grasse, P., Geilert, S., and Frank, M.: Stable silicon isotope signatures of marine pore waters – Biogenic opal dissolution versus authigenic clay mineral formation, Geochim. Cosmochim. Acta, 191, 102–117, https://doi.org/10.1016/j.gca.2016.07.022, 2016.

Elverhøi, A.: Glacigenic and associated marine sediments in the Weddell Sea, fjords of Spitsbergen and the Barents Sea: A review, Mar. Geol., 57, 53–88, https://doi.org/10.1016/0025-3227(84)90195-6, 1984.

Elverhøi, A. and Solheim, A.: The Barents Sea ice sheet - a sedimentological discussion, Polar Res., 1, 23–42, https://doi.org/10.1111/j.1751-8369.1983.tb00729.x, 1983.

Fanning, K. A. and Schink, D. R.: Interaction of Marine Sediments with Dissolved Silica, Limnol. Oceanogr., 14, 59–68, https://doi.org/10.4319/lo.1969.14.1.0059, 1969.

Faust, J. C., Stevenson, M., Abbott, G., and Knies, J.: Does Arctic warming reduce preservation of organic matter in Barents Sea sediments?, Philos. Trans. Royal Soc. A, 378, https://doi.org/10.1098/rsta.2019.0364, 2020.

Fetterer, F., Savoie, M., Helfrich, S., and Clemente-Colón, P.: Multisensor Analyzed Sea Ice Extent - Northern Hemisphere (MASIE-NH), Version 1, U.S. National Ice Center and National Snow and Ice Data Center, Boulder, Colorado USA, https://doi.org/10.7265/N5GT5K3K, 2010.

Freitas, F. S., Hendry, K. R., Henley, S. F., Faust, J. C., Tessin, A. C., Stevenson, M. A., Abbott, G. D., März, C., and Arndt, S.: Benthic-pelagic coupling in the Barents Sea: an integrated data-model framework, Philos. Trans. Royal Soc. A, 378, https://doi.org/10.1098/rsta.2019.0359, 2020.

Geilert, S., Grasse, P., Doering, K., Wallmann, K., Ehlert, C., Scholz, F., Frank, M., Schmidt, M., and Hensen, C.: Impact of ambient conditions on the Si isotope fractionation in marine pore fluids during early diagenesis, Biogeosciences, 17, 1745–1763, https://doi.org/10.5194/bg-17-1745-2020, 2020.

Gordeev, V. V., Martin, J. M., Sidorov, I. S., and Sidorova, M. V.: A reassessment of the Eurasian river input of water, sediment, major elements, and nutrients to the Arctic ocean, Am. J. Sci., 296, 664–691, https://doi.org/10.2475/ajs.296.6.664, 1996.

Hughes, H. J., Sondag, F., Santos, R. V., André, L., and Cardinal, D.: The riverine silicon isotope composition of the Amazon Basin, Geochim. Cosmochim. Acta, 121, 637–651, https://doi.org/10.1016/j.gca.2013.07.040, 2013.

Hurd, D. C.: Factors affecting solution rate of biogenic opal in seawater, Earth Planet. Sci. Lett., 15, 411–417, https://doi.org/10.1016/0012-821X(72)90040-4, 1972.

Hurd, D. C.: Interactions of biogenic opal, sediment and seawater in the Central Equatorial Pacific, Geochim. Cosmochim. Acta, 37, 2257–2282, https://doi.org/10.1016/0016-7037(73)90103-8, 1973.

Hurd, D. C., Fraley, C., and Fugate, J. K.: Silica Apparent Solubilities and Rates of Dissolution and Precipitation for ca. 25 Common Minerals at 1°-2°C, pH 7.5-8.5 in Seawater, in: Chemical Modeling in Aqueous Systems, edited by Jenne, E., chap. 21, pp. 413–445, American Chemical Society, Washington, DC, https://doi.org/10.1021/bk-1979-0093.ch021, 1979.

Jones, M. T., Pearce, C. R., and Oelkers, E. H.: An experimental study of the interaction of basaltic riverine particulate material and seawater, Geochim. Cosmochim. Acta, 77, 108–120, https://doi.org/10.1016/j.gca.2011.10.044, 2012.

Knies, J. and Stein, R.: New aspects of organic carbon deposition and its paleoceanographic implications along the Northern Barents Sea Margin during the last 30,000 years, Paleoceanography, 13, 384–394, https://doi.org/10.1029/98PA01501, 1998.

Lerman, A., Mackenzie, F. T., and Bricker, O. P.: Rates of dissolution of aluminosilicates in seawater, Earth Planet. Sci. Lett., 25, 82–88, https://doi.org/10.1016/0012-821X(75)90213-7, 1975.

Loucaides, S., Michalopoulos, P., Presti, M., Koning, E., Behrends, T., and Van Cappellen, P.: Seawater-mediated interactions between diatomaceous silica and terrigenous sediments: Results from long-term incubation experiments, Chem. Geol., 270, 68–79, https://doi.org/10.1016/j.chemgeo.2009.11.006, 2010.

Luchetta, A., Ponitz, P., and Ilyin, G.: Chemical oceanography during POLARSTERN cruise ARK-IX/4. PANGAEA, https://doi.org/10.1594/PANGAEA.927130, 2021.

Mackenzie, F. and Garrels, R.: Silicates: Reactivity with Sea Water, Science, 150, 57–58, https://doi.org/10.1126/science.150.3692.57, 1965.

Mackenzie, F. T., Garrels, R. M., Bricker, O. P., and Bickley, F.: Silica in sea water: Control by silica minerals, Science, 155, 1404–1405, https://doi.org/10.1126/science.155.3768.1404, 1967.

Maiti, K., Carroll, J. L., and Benitez-Nelson, C. R.: Sedimentation and particle dynamics in the seasonal ice zone of the Barents Sea, J. Mar. Syst., 79, 185–198, https://doi.org/10.1016/j.jmarsys.2009.09.001, 2010.

Mogollón, J. M., Dale, A. W., Fossing, H., and Regnier, P.: Timescales for the development of methanogenesis and free gas layers in recently-deposited sediments of Arkona Basin (Baltic Sea), Biogeosciences, 9, 1915–1933, https://doi.org/10.5194/bg-9-1915-2012, 2012.

Opfergelt, S. and Delmelle, P.: Silicon isotopes and continental weathering processes: Assessing controls on Si transfer to the ocean, C. R. - Geosci., 344, 723–738, https://doi.org/10.1016/j.crte.2012.09.006, 2012.

Rabouille, C., Gaillard, J. F., Tréguer, P., and Vincendeau, M. A.: Biogenic silica recycling in surficial sediments across the Polar Front of the Southern Ocean (Indian Sector), Deep. Res. II, 44, 1151–1176, https://doi.org/10.1016/S0967-0645(96)00108-7, 1997.

Rebreanu, L., Vanderborght, J. P., and Chou, L.: The diffusion coefficient of dissolved silica revisited, Mar. Chem., 112, 230–233, https://doi.org/10.1016/j.marchem.2008.08.004, 2008.

Regnier, P., O'Kane, J., Steefel, C., and Vanderborght, J.: Modeling complex multi-component reactive-transport systems: towards a simulation environment based on the concept of a Knowledge Base, Appl. Math. Model., 26, 913–927, https://doi.org/10.1016/S0307-904X(02)00047-1, 2002.

Regnier, P., Jourabchi, P., and Slomp, C. P.: Reactive-transport modeling as a technique for understanding coupled biogeochemical processes in surface and subsurface environments, Neth. J. Geosci., 82, 5–18, https://doi.org/10.1017/S0016774600022757, 2003.

Rickert, D.: Dissolution kinetics of biogenic silica in marine environments, Ph.D. thesis, Christian-Albrecht University of Kiel, 2000.

Sayles, F. L., Martin, W. R., Chase, Z., and Anderson, R. F.: Benthic remineralization and burial of biogenic SiO2, CaCO3, organic carbon, and detrital material in the Southern Ocean along a transect at 170° West, Deep. Res. II, 48, 4323–4383, https://doi.org/10.1016/S0967-0645(01)00091-1, 2001.

Siever, R.: Establishment of equilibrium between clays and sea water, Earth Planet. Sci. Lett., 5, 106–110, https://doi.org/10.1016/s0012-821x(68)80023-8, 1968.

Smedsrud, L. H., Esau, I., Ingvaldsen, R. B., Eldevik, T., Haugan, P. M., Li, C., Lien, V. S., Olsen, A., Omar, A. M., Risebrobakken, B., Sandø, A. B., Semenov, V. A., and Sorokina, S. A.: The role of the Barents Sea in the Arctic climate system, Rev. Geophys., 51, 415–449, https://doi.org/10.1002/rog.20017, 2013.

Smith, J. N., Ellis, K. M., Naes, K., Dahle, S., and Matishov, D.: Sedimentation and mixing rates of radionuclides in Barents Sea sediments off Novaya Zemlya, Deep. Res. II, 42, 1471–1493, https://doi.org/10.1016/0967-0645(95)00050-X, 1995.

Solan, M., Ward, E. R., Wood, C. L., Reed, A. J., Grange, L. J., and Godbold, J. A.: Climate-driven benthic invertebrate activity and biogeochemical functioning across the Barents Sea polar front: Climate driven benthic activity, Philos. Trans. Royal Soc. A, 378, https://doi.org/10.1098/rsta.2019.0365, 2020.

Staudigel, H., Yayanos, A., Chastain, R., Davies, G., Verdurmen, E. A., Schiffman, P., Bourcier, R., and De Baar, H.: Biologically mediated dissolution of volcanic glass in seawater, Earth Planet. Sci. Lett., 164, 233–244, https://doi.org/10.1016/S0012-821X(98)00207-6, 1998.

Sun, X., Mörth, C. M., Porcelli, D., Kutscher, L., Hirst, C., Murphy, M. J., Maximov, T., Petrov, R. E., Humborg, C., Schmitt, M., and Andersson, P. S.: Stable silicon isotopic compositions of the Lena River and its tributaries: Implications for silicon delivery to the Arctic Ocean, Geochim. Cosmochim. Acta, 241, 120–133, https://doi.org/10.1016/j.gca.2018.08.044, 2018.

Sutton, J. N., André, L., Cardinal, D., Conley, D. J., de Souza, G. F., Dean, J., Dodd, J., Ehlert, C., Ellwood, M. J., Frings, P. J., Grasse, P., Hendry, K., Leng, M. J., Michalopoulos, P., Panizzo, V. N., and Swann, G. E.: A review of the stable isotope bio-geochemistry of the global silicon cycle and its associated trace elements, Front. Earth Sci., 5, https://doi.org/10.3389/feart.2017.00112, 2018.

Thullner, M., Dale, A. W., and Regnier, P.: Global-scale quantification of mineralization pathways in marine sediments: A reaction-transport modeling approach, Geochem. Geophys. Geosystems., 10, https://doi.org/10.1029/2009GC002484, 2009.

Torres-Valdés, S., Tsubouchi, T., Bacon, S., Naveira-Garabato, A. C., Sanders, R., McLaughlin, F. A., Petrie, B., Kattner, G., Azetsu-Scott, K., and Whitledge, T. E.: Export of nutrients from the Arctic Ocean, J. Geophys. Res. Oceans, 118, 1625–1644, https://doi.org/10.1002/jgrc.20063, 2013.

Van Beusekom, J. E., Van Bennekom, A. J., Tréguer, P., and Morvan, J.: Aluminium and silicic acid in water and sediments of the Enderby and Crozet Basins, Deep. Res. II, 44, 987–1003, https://doi.org/10.1016/S0967-0645(96)00105-1, 1997.

Van Cappellen, P. and Qiu, L.: Biogenic silica dissolution in sediments of the Southern Ocean. II. Kinetics, Deep. Res. II, 44, 1129–1149, https://doi.org/10.1016/S0967-0645(96)00112-9, 1997.

Van Cappellen, P., Dixit, S., and van Beusekom, J.: Biogenic silica dissolution in the oceans: Reconciling experimental and field-based dissolution rates, Global Biogeochem. Cycles, 16, 23–1–23–10, https://doi.org/10.1029/2001gb001431, 2002.

Ward, J., Hendry, K., Arndt, S., Faust, J., Freitas, F., Henley, S. F., Krause, J., Maerz, C., Ng, H. C., and Pickering, R.: Stable Silicon Isotopes Uncover a Mineralogical Control on the Benthic Silicon Cycle in the Arctic Barents Sea, Geochim. Cosmochim. Acta, 329, 206–230, https://doi.org/10.1016/j.gca.2022.05.005, 2022.

Wetzel, F., de Souza, G. F., and Reynolds, B. C.: What controls silicon isotope fractionation during dissolution of diatom opal?, Geochim. Cosmochim. Acta, 131, 128–137, https://doi.org/10.1016/j.gca.2014.01.028, 2014.

Zaborska, A., Carroll, J. L., Papucci, C., Torricelli, L., Carroll, M. L., Walkusz-Miotk, J., and Pempkowiak, J.: Recent sediment accumulation rates for the Western margin of the Barents Sea, Deep. Res. II, 55, 2352–2360, https://doi.org/10.1016/j.dsr2.2008.05.026, 2008.

Zhu, C., Liu, Z., Zhang, Y., Wang, C., Scheafer, A., Lu, P., Zhang, G., Georg, R. B., lin Yuan, H., and Rimstidt, J. D.: Measuring silicate mineral dissolution rates using Si isotope doping, Chem. Geol., 445, 146–163, https://doi.org/10.1016/j.chemgeo.2016.02.027, 2016.

Ziegler, K., Chadwick, O. A., Brzezinski, M. A., and Kelly, E. F.: Natural variations of $\delta 30Si$ ratios during progressive basalt weathering, Hawaiian Islands, Geochim. Cosmochim. Acta, 69, 4597–4610, https://doi.org/10.1016/j.gca.2005.05.008, 2005a.

Ziegler, K., Chadwick, O. A., White, A. F., and Brzezinski, M. A.: $\delta 30Si$ systematics in a granitic saprolite, Puerto Rico, Geology, 33, 817–820, https://doi.org/10.1130/G21707.1, 2005b.